EES Solar

PAPER

View Article Online
View Journal | View Issue

Cite this: *EES Sol.*, 2025, **1**, 1115

Quartz wool-supported porphyrin supramolecular photocatalysts for robust and scalable H_2O_2 generation

Ji Liu,[a] Wenting Qiu,[a] Shuai Dou,[a] Hengjun Shang,[a] Yaning Zhang,[a] Jing Xu,[b] Jiawei Zhang,[a] Yang Lou,[a] Ying Zhang,[a] Yongfa Zhu[c] and Chengsi Pan*[ab]

Achieving stable immobilization of organic photocatalysts is essential for practical photocatalytic hydrogen peroxide (H_2O_2) production. In this study, we propose a robust photocatalytic strategy that immobilizes self-assembled porphyrin nanosheets (SA-TCPP) onto quartz wool (QW), using polydimethylsiloxane (PDMS) as both a binding and encapsulating medium. By optimizing the viscosity and operating temperature of PDMS, the resulting PDMS/SA-TCPP/QW composite achieves a high H_2O_2 yield of 95 μmol and maintains excellent stability over 10 cycles. The composite reaches a concentration of 7.4 mM and an internal quantum efficiency as high as 15.84% at 420 nm, which is comparable to that of SA-TCPP powder. In a modular flow reactor, it produced 3.5 mmol of H_2O_2 over 50 h, with the final solution concentrated to 100 mM, demonstrating strong scalability. In the PDMS/SA-TCPP/QW composite, PDMS forms a semi-solid interfacial layer that not only physically anchors the SA-TCPP nanosheets but also enhances interfacial stability through the formation of covalent amide (–CONH–) bonds. This integrated design offers a practical and broadly applicable strategy for the stable immobilization of organic photocatalysts.

Received 15th September 2025
Accepted 19th October 2025

DOI: 10.1039/d5el00147a

rsc.li/EESSolar

Broader context

Photocatalytic H_2O_2 production represents a sustainable approach because it relies on environmentally benign water, oxygen, and sunlight. However, most existing photocatalytic systems are designed in powder-suspension form, which typically suffers from limited reusability, challenging recovery, and poor dispersion. In this study, polydimethylsiloxane (PDMS) is employed as a semi-solid interfacial binder to immobilize porphyrin nanosheets (SA-TCPP) onto quartz wool (QW). This immobilization strategy enables the preparation of a PDMS/SA-TCPP/QW composite that achieves a high H_2O_2 production rate of 1.8 mM h^{-1}, comparable to the performance of the powder counterpart. Moreover, the system can be readily scaled up, with activity increasing proportionally as the number of loaded QW modules increases from 1 to 8, and demonstrates excellent operational stability for up to 50 h. QW proves to be an ideal support due to its chemical inertness toward H_2O_2 and its highly porous fibrous network, which provides efficient dispersion of active SA-TCPP photocatalysts. Meanwhile, PDMS effectively stabilizes the immobilized SA-TCPP and maintains its dispersity, attributed to its high viscosity and strong chemical interactions. Overall, this strategy offers a practical route toward modular, continuous-flow photocatalytic systems and underscores the potential of decentralized solar-driven chemical manufacturing.

1. Introduction

Hydrogen peroxide (H_2O_2) is a versatile and environmentally benign oxidant, widely employed in healthcare, food processing, environmental remediation, and chemical synthesis. Its sole decomposition products, water and oxygen, render it particularly attractive for sustainable chemistry.[1,2] Currently, industrial H_2O_2 is produced *via* the anthraquinone (AQ) process, which involves sequential hydrogenation and oxidation steps catalysed by Pd complexes.[3,4] Despite its commercial viability, this process is energy-intensive, generates hazardous waste, and poses challenges in H_2O_2 storage and transport due to its intrinsic instability. To address the limitations associated with conventional H_2O_2 production and distribution, decentralized H_2O_2 generation has emerged as a promising strategy, enabling on-demand synthesis at the point of use.[5–7] Among the various methods under exploration, photocatalysis stands out as a green and solar-driven alternative. In principle, it requires only water, oxygen, and a semiconductor photocatalyst, providing a direct and sustainable pathway to H_2O_2.[8,9]

[a]*International Joint Research Center for Photoresponsive Molecules and Materials, School of Chemical and Material Engineering, Jiangnan University, Wuxi, Jiangsu, 214122, China. E-mail: cspan@jiangnan.edu.cn*

[b]*School of Food Science and Technology, Jiangnan University, Wuxi, Jiangsu, 214122, China*

[c]*Department of Chemistry, Tsinghua University, Beijing, 100086, China*

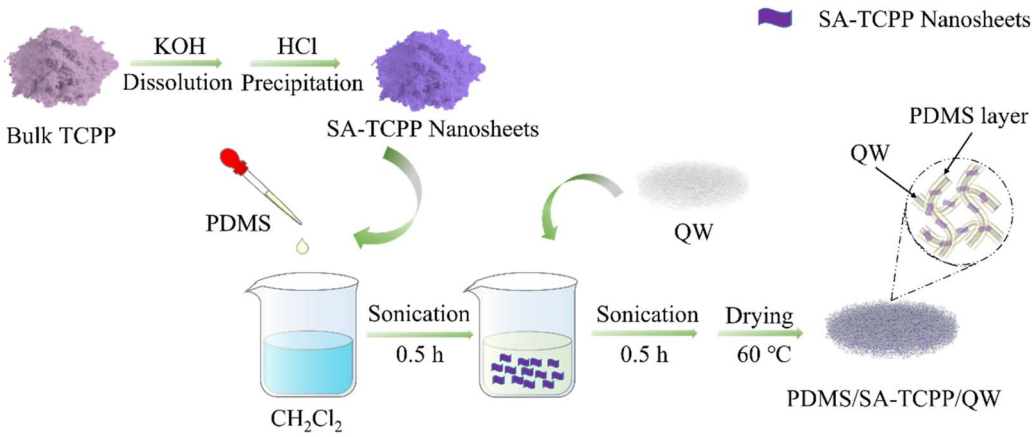

Fig. 1 Schematic of the preparation process of QW loaded with SA-TCPP nanosheets.

To date, various organic photocatalysts (*e.g.*, g-C_3N_4 (ref. 10 and 11) and porphyrins[12,13]) have been studied for photocatalytic H_2O_2 production. However, they are mostly used in powder form, which limits their practical applications due to poor reusability, difficult recovery, and inadequate dispersion. Also, such photocatalyst-suspended systems remain largely confined to laboratory-scale investigations. These limitations have sparked increasing interest in photocatalyst immobilization as a means to enable reactor integration, long-term operational stability, and continuous-flow operation. Immobilization improves photocatalyst reusability and simplifies separation and recycling.[14,15] Despite these benefits, immobilization still presents significant challenges. Achieving strong adhesion between the photocatalyst and support without compromising activity remains a major difficulty. Hence, selecting a suitable support material is critical—it must offer high surface area, robust physicochemical stability, and strong interfacial interaction with the photocatalyst.

In recent years, some organic support materials have been investigated for H_2O_2 production, including polymers,[16,17] metal organic frameworks (MOFs),[18,19] and covalent organic frameworks (COFs).[20,21] However, these organic supports suffer from high cost and poor chemical stability in the produced H_2O_2 solution. Although some inorganic supports have been reported, such as glass beads,[22] and porous alumina ceramics,[23] these inorganic supports exhibit a small surface area, resulting in much lower photocatalytic performance for the immobilized system compared to the corresponding powder suspension. Given the above limitations, quartz wool (QW) emerges as an ideal support for photocatalyst immobilization, owing to its excellent thermal stability, chemical inertness, high optical transparency, and highly porous fibrous network.[24,25] For instance, nanoscale TiO_2 layers have been reported to be deposited on QW surfaces by sol–gel methods, resulting in good adhesion and uniform morphology.[26,27] However, the immobilization is primarily suited for inorganic photocatalysts, which can readily interact with hydroxylated surfaces. The highly active organic photocatalysts in the H_2O_2 production field typically exhibit poor affinity toward the QW surface and have been insufficiently explored. The stable immobilization of organic H_2O_2-production photocatalysts onto QW remains challenging.

Polydimethylsiloxane (PDMS)[28,29] offers a unique combination of chemical inertness in H_2O_2, high optical transparency, excellent thermal and photostability, inherent gas-permeability and coating flexibility. In the literature, the material has been used as an encapsulation medium or support matrix.[30–32] Therefore, the material may be used as a binder to increase the affinity between the support and organic H_2O_2 production photocatalysts.

Self-assembled tetrakis(4-carboxyphenyl) porphyrin (SA-TCPP) nanosheets are reported as one of the highest-activity photocatalysts by our group.[33,34] However, the material is only studied in its powder form, which limits further utilization. To achieve stable immobilization of the SA-TCPP photocatalyst, we propose a PDMS-coating strategy to immobilize SA-TCPP onto QW for scalable H_2O_2 production by an evaporation method (Fig. 1). The control factors of the supported system on the H_2O_2 production activity are studied. The effect of PDMS coating in stabilizing the SA-TCPP photocatalysts on QW and in enhancing H_2O_2 production activity is clarified. Furthermore, we report that the introduction of amino-functionalized PDMS (NH_2-PDMS) enables the formation of amide linkages with the carboxyl groups of SA-TCPP, significantly enhancing its overall stability, with H_2O_2 concentration reaching 7.4 mM. This strategy enables robust and scalable H_2O_2 production using immobilized organic photocatalysts.

2. Results and discussion

2.1 Morphological and structural characterizations

The morphology of the prepared samples is investigated using SEM. Fig. 2a–d present the SEM images of QW, PDMS/QW, SA-TCPP/QW, and PDMS/SA-TCPP/QW composites, respectively, illustrating the stepwise modification process and corresponding morphological changes. Fig. 2a shows that the single QW fiber exhibits a rough and uniform surface with a diameter of approximately 2.5 μm. Multiple fibers are intertwined to form a three-dimensional porous network (Fig. S1a), which serves as a potential substrate for SA-TCPP nanosheets loading.

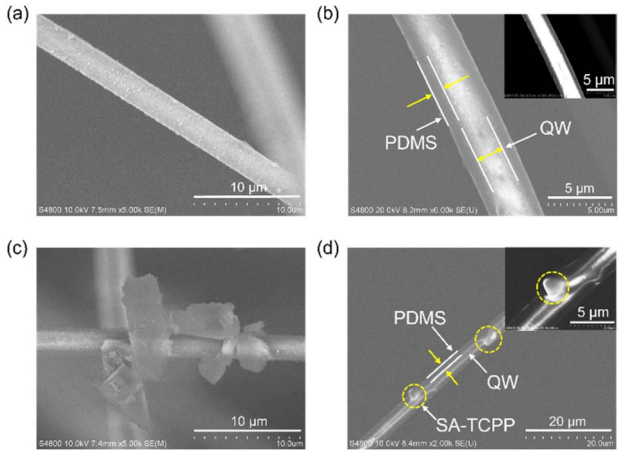

Fig. 2 SEM images of (a) QW, (b) PDMS/QW composite (b inset, corresponding BSE image), (c) SA-TCPP/QW composite, and (d) PDMS/SA-TCPP/QW composite (d inset, corresponding BSE image).

Fig. 2b shows the morphology of QW modified with PDMS alone, which exhibits a smooth and uniform surface. In this case, PDMS is found to uniformly coat the surface of QW with a thickness of approximately 1 μm. The backscattered electron (BSE) image in Fig. 2b reveals a distinct contrast between the PDMS layer and the QW substrate, indicating clear phase separation. Since BSE imaging is sensitive to differences in atomic number, the brighter QW core and darker PDMS shell provide direct evidence for the successful formation of a PDMS-coated layer. This contrast confirms the presence and uniformity of the PDMS coating. Compared to Fig. 2a, this demonstrates that PDMS forms a distinguishable layer, potentially improving surface adhesion for subsequent SA-TCPP catalyst deposition.

Fig. 2c shows the morphology of SA-TCPP loaded onto QW. After loading, SA-TCPP nanosheets are observed outside the surface of QW. The SA-TCPP nanosheets are also confirmed by the SEM observation without the addition of QW and PDMS (Fig. S1b). Note that some nanosheets are only partially in contact with QW, indicating the weak interaction between them. This may affect the mechanical stability during the reaction.

Fig. 2d shows PDMS-coated QW with SA-TCPP nanosheets. SA-TCPP nanosheets are still observed on the surface of QW fibers with an average diameter of 3 μm. On the outermost surface, a thin layer of PDMS is observed, which covers the surfaces of both QW and SA-TCPP. In the corresponding backscattered electron (BSE) image, the QW core appears brightest due to its high atomic number constituents (Si and O). The SA-TCPP nanosheets also show relatively high brightness, which can be attributed to their multi-layered, densely stacked morphology formed *via* π–π self-assembly, resulting in enhanced electron backscattering. In contrast, the PDMS coating appears darker, consistent with its low density, thin-film structure, and lower average atomic number. These contrast differences clearly reveal the spatial arrangement and phase separation within the composite. Incorporating a PDMS interlayer can reinforce interfacial adhesion between SA-TCPP and QW, thereby enhancing mechanical integrity during photocatalytic operation.

The interaction among the QW, PDMS, and SA-TCPP is investigated by FTIR spectra as shown in Fig. 3a. For the PDMS/SA-TCPP/QW composite, a broad and weak absorption band

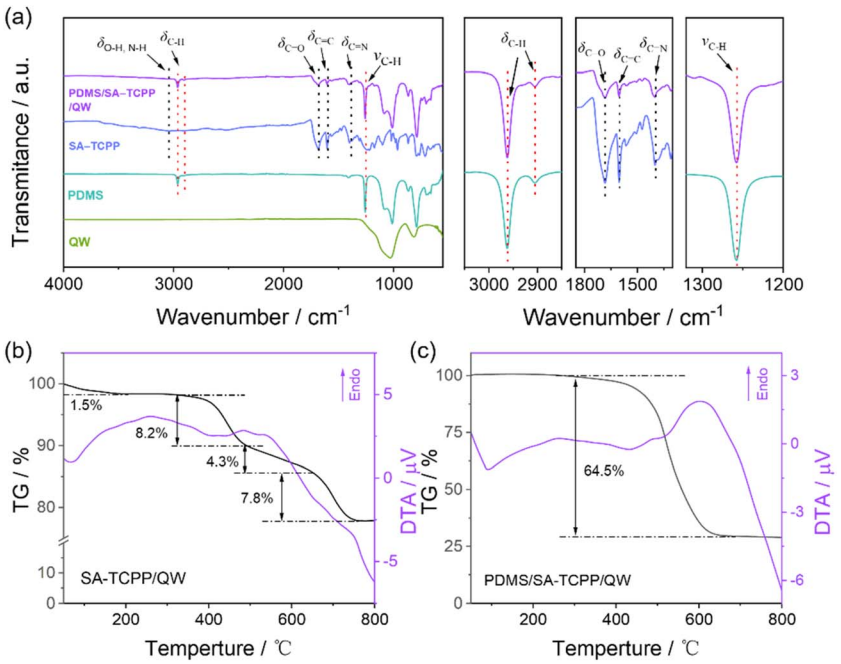

Fig. 3 (a) FTIR spectra of PDMS/SA-TCPP/QW composite, SA-TCPP, PDMS, and QW, along with enlarged views comparing SA-TCPP and PDMS with the PDMS/SA-TCPP/QW composite. TG-DTA curves of (b) SA-TCPP/QW composite and (c) PDMS/SA-TCPP/QW composite.

appears in the range of 2500–3300 cm^{-1}, corresponding to O–H and N–H stretching vibrations. Sharp peaks at 1684 cm^{-1}, 1602 cm^{-1}, and 1402 cm^{-1} are attributed to the stretching modes of C=O, C=C, and C=N, respectively.[35,36] These peaks indicate that SA-TCPP is well preserved within the composite as compared with the FTIR spectrum of pure SA-TCPP.

The absorption bands at 2962 cm^{-1} and 2902 cm^{-1} correspond to the symmetric and asymmetric C–H stretching vibrations of methyl groups, while those at 1411 cm^{-1} and 1258 cm^{-1} are assigned to their in-plane and out-of-plane bending vibrations. The peaks at 862 cm^{-1} and 786 cm^{-1} are ascribed to the stretching and bending vibrations of Si–C bonds,[37,38] confirming the presence of the PDMS siloxane backbone in the supported system.

Additionally, the broad absorption band observed between 750 cm^{-1} and 1350 cm^{-1} is characteristic of Si–O–Si stretching vibrations of amorphous SiO_2,[25,39] verifying the presence of the QW support. Note that the characteristic peaks in the PDMS/SA-TCPP/QW composite are retained without significant shifts or new absorption bands relative to that of SA-TCPP, PDMS, and QW, indicating the absence of chemical bonding among the components. Instead, the composite is stabilized mainly because of physical interactions. PDMS may act as a semi-solid encapsulating medium,[40,41] embedding SA-TCPP and adhering to the QW surface. This interfacial structure spatially stabilizes the SA-TCPP without disrupting its electronic structure, thereby preserving its photocatalytic activity. Notably, UV-Vis-NIR spectroscopy (Fig. S2) reveals that the introduction of PDMS does not alter the light absorption profile of SA-TCPP, indicating that PDMS is optically transparent in the 350–1000 nm range.

Fig. 3b presents the TG and DTA curves of the SA-TCPP/QW composite. The TG curves reveal a multistep decomposition process, exhibiting thermal behaviour similar to that of SA-TCPP (Fig. S3a). The mass loss before 600 °C is approximately 77.0%, which is attributed to the thermal decomposition of SA-TCPP, whereas QW exhibits negligible mass loss below this temperature (Fig. S3b). In comparison, pure SA-TCPP exhibits a mass loss of 88.0% below 600 °C. The additional mass loss of SA-TCPP in the SA-TCPP/QW composite beyond 600 °C is estimated to be 10.5%. Meanwhile, QW alone exhibits a mass loss of approximately 12.5%. These results indicate that the thermal decomposition characteristics of SA-TCPP are preserved in the SA-TCPP/QW composite, with QW serving as an inert support with negligible influence on the overall decomposition process.

After the introduction of PDMS, the TG curve of the PDMS/SA-TCPP/QW composite (Fig. 3c) exhibits initial decomposition characteristics similar to those of SA-TCPP. This suggests a lack of covalent bonding between PDMS and SA-TCPP. However, its final decomposition temperature is identical to that of PDMS (Fig. S3c). Notably, no further weight loss of SA-TCPP is observed beyond 600 °C, in contrast to the SA-TCPP/QW composite. Thus, PDMS enhances the overall thermal stability of the system. Moreover, these decomposition characteristics indicate that PDMS likely forms a dense, thermally stable coating. This physical encapsulation effect is supported by SEM imaging, which reveals a uniform PDMS coating on the composite surface (Fig. 2d).

FTIR analysis confirms the preservation of SA-TCPP's structural integrity and the physical adsorption effect of PDMS in the PDMS/SA-TCPP/QW composite. In addition, TG and DTA analyses demonstrate that PDMS significantly enhances the thermal stability of the composite.

2.2 Photocatalytic H_2O_2 production on PDMS/SA-TCPP/QW

The photocatalytic H_2O_2 production on the PDMS/SA-TCPP/QW composite is evaluated in pure water under 4 h of visible light irradiation, showing the highest activity under pure water conditions (Fig. S4). The activities of PDMS, PDMS/QW, and SA-TCPP/QW composites are also evaluated as controls (Fig. 4a and S5a). The PDMS/SA-TCPP/QW composite produces 30 μmol of H_2O_2 after 4 h. In contrast, both pure PDMS and PDMS/QW show negligible amounts of H_2O_2 production under the same conditions. This suggests that the observed activity of the PDMS/SA-TCPP/QW composite does not originate from either PDMS or QW. Meanwhile, the SA-TCPP/QW composite produces 12 μmol of H_2O_2 over 4 h, which is only one-third relative to that of the PDMS/SA-TCPP/QW composite. This significant increase highlights the advantage of incorporating PDMS in the supported system. Additionally, the optimal mass ratio of SA-TCPP to PDMS is determined to be 1 : 6 (Fig. S5b).

The time-dependent H_2O_2 production on SA-TCPP/QW and PDMS/SA-TCPP/QW composites is detailed in Fig. 4b. At the initial stage of the reaction, SA-TCPP/QW exhibits significantly higher H_2O_2 activity than PDMS/SA-TCPP/QW, which can be attributed to the diffusion resistance of O_2 introduced by the PDMS layer (*vide infra*). However, after 27 min, the H_2O_2 production rate of the PDMS/SA-TCPP/QW composite surpasses that of SA-TCPP/QW, reaching 9 μmol after 1 h, whereas the latter achieves only 7 μmol.

To elucidate the effect of PDMS on the performance differences between the two composites, we compare the optical microscopy images and photos of SA-TCPP/QW and PDMS/SA-TCPP/QW composites before and after the photocatalytic reaction (Fig. 4c and S6). Before the reaction, the SA-TCPP/QW composite surface is densely covered with aggregated SA-TCPP nanosheets. After the reaction, however, a large amount of SA-TCPP detachment is observed, with most nanosheets missing and large areas of the QW surface exposed, corresponding to the extent of SA-TCPP detachment. This suggests insufficient interfacial adhesion and poor structural integrity under photocatalytic conditions, leading to catalyst shedding and decreased H_2O_2 production performance.

In contrast, the PDMS/SA-TCPP/QW composite maintains a uniform distribution of SA-TCPP nanosheets before and after the reaction, with no visible structural detachment. Consequently, its H_2O_2 production continues to improve with extended reaction time. These results indicate that PDMS plays a critical role in maintaining the structural integrity of the composite during the photocatalytic process, which accounts for the observed differences in catalytic performance.

In the absence of PDMS, SA-TCPP lacks effective adhesion to the QW surface and is susceptible to detachment into the solution, leading to significant SA-TCPP loss. In contrast, the

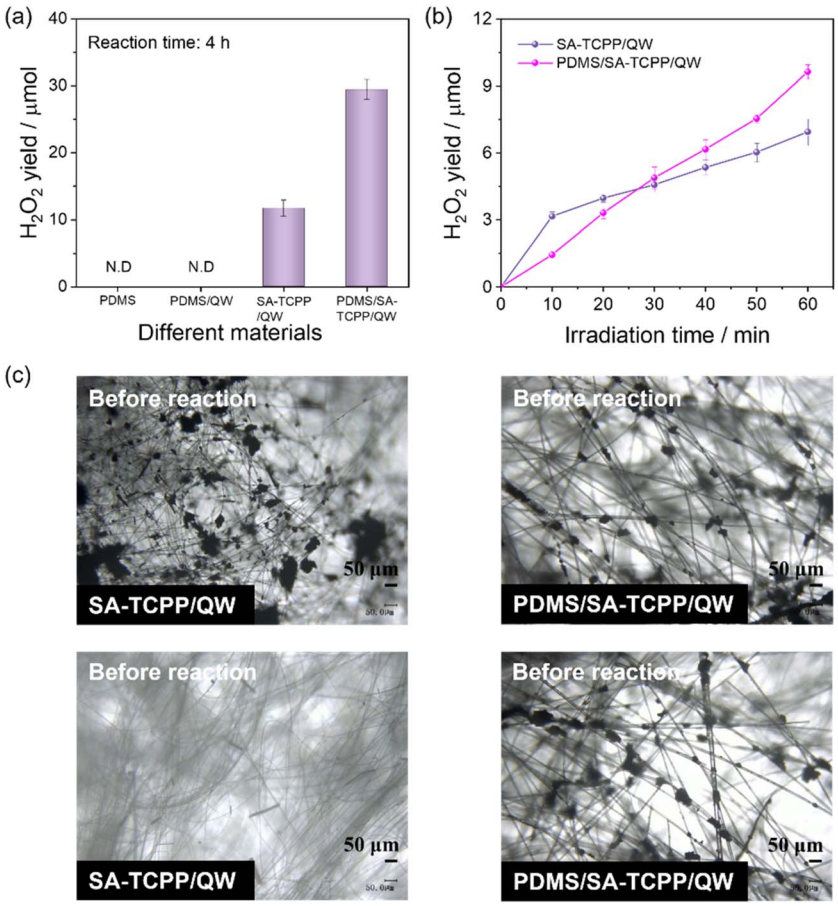

Fig. 4 (a) H_2O_2 production on the PDMS, PDMS/QW, SA-TCPP/QW, and PDMS/SA-TCPP/QW composites. (b) H_2O_2 yields of SA-TCPP/QW and PDMS/SA-TCPP/QW composites for 1 h. (c) Optical microscopy images of the SA-TCPP/QW and PDMS/SA-TCPP/QW composites before and after photocatalytic reaction. Solution: 30 mL H_2O, pH = 7, temperature: 40 °C, SA-TCPP catalyst loading: 45 mg, O_2 bubbling, light source: Xe lamp with a 420 nm cut-off filter.

incorporation of PDMS contributes to improved overall stability. Contact angle measurements show a value of 110° (Fig. S7), confirming the pronounced hydrophobicity of PDMS. The inherent viscosity of PDMS also enhances the adhesion between SA-TCPP and the QW substrate, while also promoting a more uniform dispersion of SA-TCPP across the QW surface. The above factors act synergistically to stabilize the distribution of the SA-TCPP catalyst and maintain its photocatalytic activity.

The effect of reaction temperature on the H_2O_2 production activity is further investigated. In our previous study, reaction temperature is identified as a critical parameter influencing H_2O_2 generation, as elevated temperatures promote the hydrolysis of peroxyl acids—formed by photogenerated holes—into H_2O_2, thereby inhibiting the accumulation of peroxyl acid recombination centres. For the SA-TCPP powder photocatalyst, the optimal temperature is previously determined to be 80 °C.

In the current study, a range of temperatures from 20 °C to 80 °C are tested to evaluate the influence of thermal conditions on H_2O_2 production activity of the PDMS/SA-TCPP/QW composite, as shown in Fig. 5a. We also evaluate the cycling stability of the composite across six consecutive runs at each temperature. As the reaction temperature increases from 20 °C to 80 °C, the H_2O_2 yield after 4 h increased from 19 μmol to 58 μmol. However, this improvement in activity is accompanied by a significant decline in cycling stability at 60 °C and 80 °C. In contrast, the composite demonstrates excellent durability at 20 °C and 40 °C. Considering both photocatalytic activity and cycling stability, 40 °C is identified as the optimal reaction temperature. Under this condition, PDMS/SA-TCPP/QW composite produces 30 μmol of H_2O_2 after 4 h reaction and retains 90% of its initial activity after six cycles. Also, negligible structure change is found on the composite after six cycles (Fig. S8).

To study the reasons for rapid activity fade at elevated temperatures, the residual amount of SA-TCPP and corresponding photographs of PDMS/SA-TCPP/QW composite before and after photocatalytic reactions at 40 °C and 80 °C are presented in Fig. 5b. At 40 °C, the PDMS/SA-TCPP/QW composite retains 90% of its initial SA-TCPP content (from 45 mg to 38 mg), with negligible visual change, indicating strong structural integrity and effective anchoring of the SA-TCPP catalyst. In contrast, at 80 °C, a dramatic loss of SA-TCPP is observed, with the remaining amount dropping to only 12 mg (27% retention), accompanied by a significant color change from purple to pale,

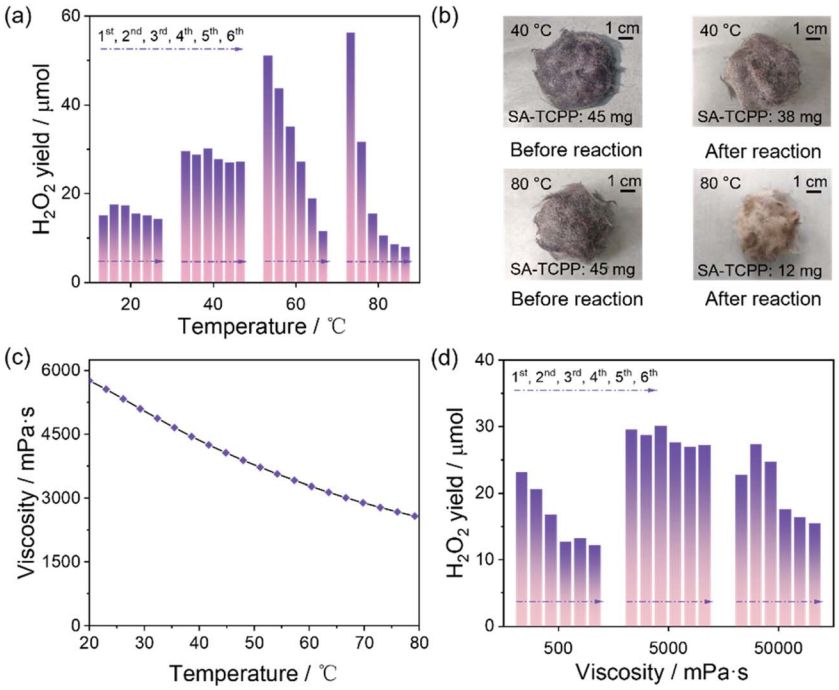

Fig. 5 (a) H_2O_2 yields and cycling stability of PDMS/SA-TCPP/QW composites at various reaction temperatures (PDMS viscosity: 5000 mPa s). (b) Corresponding macroscopic photographs of PDMS/SA-TCPP/QW composite before and after reactions at 40 °C and 80 °C, illustrating the morphological changes under thermal conditions. (c) Temperature-dependent viscosity profile of PDMS (5000 mPa s) under atmospheric pressure. (d) H_2O_2 yields and cycling stability of PDMS/SA-TCPP/QW composite at various PDMS viscosities. Reaction temperature: 40 °C. Solution: 30 mL H_2O, pH = 7, SA-TCPP catalyst loading: 45 mg, O_2 bubbling, reaction time: 4 h, light source: Xe lamp with a 420 nm cut-off filter.

suggesting severe detachment of the active layer. This stark contrast highlights the critical role of temperature in determining PDMS/SA-TCPP/QW composite stability. The elevated temperature likely reduces the viscosity of the PDMS matrix, weakening its physical adhesion to SA-TCPP, thereby accelerating the loss of the catalytic layer.

We then measure the temperature-dependent viscosity variation of PDMS to elucidate the reason for the detachment of SA-TCPP from QW at elevated temperatures. Fig. 5c shows rheological measurements of PDMS in the range from 20 °C to 80 °C. The results show an inverse relationship between temperature and PDMS viscosity. Accordingly, the fluidity of PDMS increases with temperature, which weakens its physical interaction with the surface-bound SA-TCPP. This suggests that elevated temperatures cause the semi-solid PDMS to flow away from the encapsulated SA-TCPP, resulting in its detachment into the solution.

The viscosity of PDMS with distinct differences is further studied in the supported system. Three PDMS viscosities (500 mPa s, 5000 mPa s, and 50 000 mPa s) are chosen, and the photocatalytic activity is also evaluated for six cycles (Fig. 5d). At a PDMS viscosity of 500 mPa s, the accumulated amount of H_2O_2 reaches 22 μmol after 4 h of reaction. However, after six cycles, it rapidly decays to 12 μmol, confirming the importance of the PDMS viscosity to activity stability. Besides that, the SEM images show that PDMS visibly aggregates on QW at a viscosity of 500 mPa s (Fig. S9), which may also decrease the activity. At viscosities of 5000 and 50 000 mPa s, the accumulated amounts of H_2O_2 reach 30 μmol and 23 μmol, respectively. After six cycles, the activity stabilizes at approximately 90% and 65% relative to their first run, respectively. Note that the accumulation amount of H_2O_2 for the latter is slightly lower than that of the former. This may be due to the slow O_2 diffusion in the PDMS with a high viscosity (0.4×10^{-9} m^2 s^{-1}, 50 000 mPa s) relative to the one with a low viscosity (2.2×10^{-9} m^2 s^{-1}, 5000 mPa s) (SI Note S1, Table S1 and Fig. S10). The slow O_2 diffusion in the PDMS layer may limit the H_2O_2 generation rate at high PDMS viscosity. In addition to O_2 diffusion, the diffusion coefficients of H_2O_2 (2.2×10^{-8} m^2 s^{-1}, SI Note S2 and Fig. S11), and H_2O (6.8×10^{-8} m^2 s^{-1}, SI Note S3 and Fig. S12) in the medium-viscosity PDMS layer are also measured, revealing that both species readily permeate through the PDMS layer. This finding confirms that water molecules access the encapsulated SA-TCPP photocatalyst, while the generated H_2O_2 diffuses outward into the aqueous phase, thereby sustaining the photocatalytic reaction.

Medium-viscosity PDMS (5000 mPa s) provides optimal physical fixation of SA-TCPP and oxygen diffusivity, ensuring high photocatalytic activity and excellent reusability under mild conditions.

2.3. Enhancement of the activity and durability of H_2O_2 production on PDMS/SA-TCPP/QW composite *via* amidation

We further investigate the effect of PDMS type on the H_2O_2 production activity. Fig. 6a shows the H_2O_2 production using PDMS with three terminal groups: –NH_2 (NH_2-PDMS), –OH (HO-

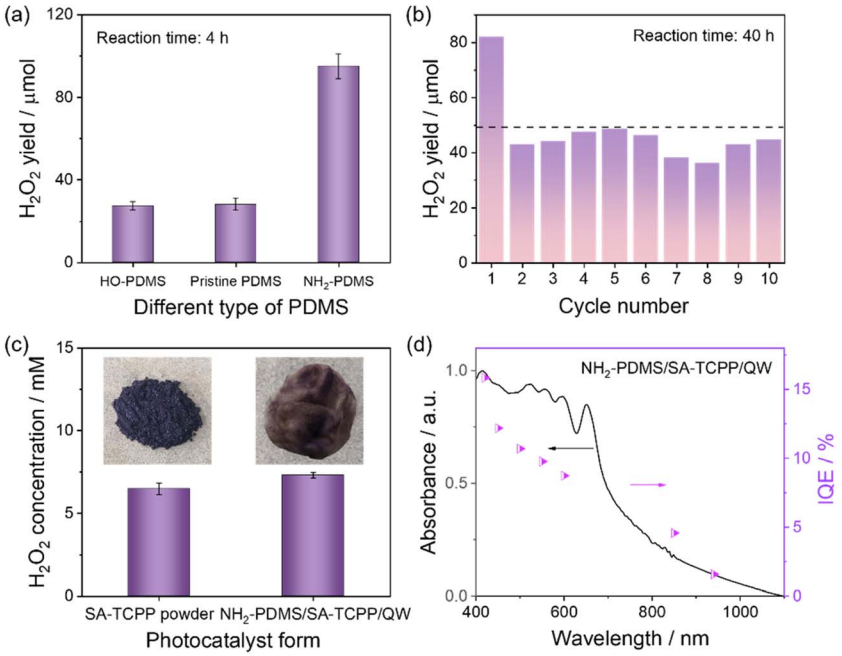

Fig. 6 (a) Comparison of the H_2O_2 yields for pristine PDMS/SA-TCPP/QW, HO-PDMS/SA-TCPP/QW, and NH_2-PDMS/SA-TCPP/QW composites. (b) Cycling stability of the NH_2-PDMS/SA-TCPP/QW composite over ten successive runs. (c) Comparison of the H_2O_2 yields between SA-TCPP powder and NH_2-PDMS/SA-TCPP/QW composite at 80 °C. (Insets) Photographs showing the SA-TCPP powder (left) and the immobilized NH_2-PDMS/SA-TCPP/QW composite (right). (d) UV-Vis-NIR absorption spectrum (black line, left axis) and incident quantum efficiency (IQE, magenta triangles, right axis) of NH_2-PDMS/SA-TCPP/QW composite under irradiation with different monochromatic wavelengths. Solution: 30 mL H_2O, pH = 7, temperature: 40 °C, SA-TCPP catalyst loading: 45 mg, O_2 bubbling, reaction time: 4 h, light source: Xe lamp with a 420 nm cut-off filter.

PDMS), and $-CH_3$ (pristine PDMS). Among the tested types of PDMS, the H_2O_2 production of the NH_2-PDMS/SA-TCPP/QW composite reaches up to 95 μmol, approximately three times higher than that of HO-PDMS/SA-TCPP/QW and pristine PDMS/SA-TCPP/QW composites (around 30 μmol for each sample). NH_2-PDMS markedly enhances the photocatalytic H_2O_2 production. A control test confirms that NH_2-PDMS/QW alone is inactive for H_2O_2 generation, indicating that the photocatalytic activity of NH_2-PDMS/SA-TCPP/QW originates solely from SA-TCPP (Fig. S13). The presence of the amino terminal group is essential for enhancing the photocatalytic efficiency of the PDMS/SA-TCPP/QW composite.

To investigate the origin of high H_2O_2 accumulation with NH_2-PDMS, FTIR spectra of the PDMS/SA-TCPP/QW and NH_2-PDMS/SA-TCPP/QW composites are obtained and compared (Fig. S14a). The C=O stretching vibration is found to shift from 1684 cm^{-1} in SA-TCPP to 1700 cm^{-1} in NH_2-PDMS/SA-TCPP/QW composite. This shift is attributed to the formation of covalent amide bonds (–CONH–) between the amino groups of NH_2-PDMS and the carboxylic acid groups of SA-TCPP. In addition, we compare the ^{13}C NMR spectra of SA-TCPP and NH_2-PDMS modified SA-TCPP. Compared with pristine SA-TCPP, a new resonance signal appears at 173.8 ppm after NH_2-PDMS modification, corresponding to the carbonyl carbon of the amide group (Fig. S14b), which is consistent with previous reports.[36,42–44] Such additional covalent interactions may work synergistically with the intrinsic physical interactions of PDMS, inhibiting the detachment of SA-TCPP from the QW surface. The resulting steady H_2O_2 production accounts for the high accumulation, resembling the trend observed in SA-TCPP/QW systems with and without PDMS (Fig. 4b).

We also evaluate the durability of the NH_2-PDMS/SA-TCPP/QW composite. The activity tests are carried out over ten consecutive cycles of H_2O_2 generation, each lasting 4 h under identical conditions (Fig. 6b). The initial H_2O_2 production is 80 μmol and stabilizes at 44 μmol in the subsequent cycles, remaining approximately 1.5 times higher than that of pristine-PDMS/SA-TCPP/QW composite. We collect and quantify the amount of SA-TCPP detached after each photocatalytic cycle (Table S2). A significant loss of 9 mg (*ca.* 20%) is detected in the first cycle, while the variation in subsequent cycles is negligible. The initial activity enhancement is attributed to loosely bound or unstable SA-TCPP, which detaches during the first cycle. Thereafter, the system maintains consistent performance and structural integrity. The composite also exhibits a continuous increase in H_2O_2 yield over 50 h of visible light irradiation, ultimately reaching 360 μmol (Fig. S15).

Next, we compare the NH_2-PDMS/SA-TCPP/QW composite with SA-TCPP powder. The composite produces 7.4 mM of H_2O_2 within 4 h, with comparable activity to SA-TCPP powder (6.4 mM) (Fig. 6c). In addition, the NH_2-PDMS/SA-TCPP/QW composite achieved an H_2O_2 concentration of 3.2 mM under simulated sunlight (AM 1.5G), comparable to the powders reported under the same conditions[34] (Fig. S16). This is

encouraging for scalability study because in most photocatalytic cases, the suspension system always exhibits much higher activity than the supported system due to a larger reactive surface area. More importantly, the amount of H_2O_2 produced on NH_2-PDMS/SA-TCPP/QW composite ranks among the highest compared with other supported photocatalysts reported in the literature (Table S3). The internal quantum efficiency (IQE) and H_2O_2 yields of the NH_2-PDMS/SA-TCPP/QW composite at various wavelengths are also evaluated. The resulting IQE is consistent with the UV-Vis-NIR absorption spectrum (Fig. 6d, SI Note S4 and Fig. S17), indicating that the H_2O_2 production is due to the photocatalytic process. The highest IQE is observed at 420 nm, reaching 15.84%, compared with other top-performing suspended powder systems (*ca.* 20%).[45]

2.4 Conceptual verification for scale-up H_2O_2 production using multiple supported SA-TCPP modules

Encouraged by the high H_2O_2 production efficiency of single NH_2-PDMS/SA-TCPP/QW module, we carry out photocatalytic tests with multiple QW modules. The device design is shown in Fig. 7a. A cylindrical quartz reactor with an inner irradiation-type is used with 25 cm in height and 5 cm in inner diameter (see the photo in Fig. 7a). A 24 cm-long arc Xe lamp is employed as the visible light source with cooling water to control the reaction temperature at 40 °C. Multiple QW modules are placed between the light source and inner wall of the quartz reactor, each measuring 10 cm in length and 7 cm in width. The detailed configuration of the experimental setup is illustrated in Fig. S18.

Fig. 7b shows the H_2O_2 production with increasing the NH_2-PDMS/SA-TCPP/QW modules. As the number of QW modules increases from 1 to 8, the H_2O_2 production rate nearly increases at the same ratio. When the number is 8, the H_2O_2 production amount reaches up to 450 μmol after 4 h of irradiation. When the O_2 saturated condition switches to the air condition, the H_2O_2 yield still maintains at 350 μmol (Fig. 7c), corresponding to approximately 70% of that obtained under pure oxygen. This high accumulation at the air conditions indicates the potential use of the supported system at the ambient atmosphere.

We then evaluate the H_2O_2 accumulation during a continuous reaction over 50 h. In this case, the cumulative H_2O_2 production reaches 3.5 mmol with almost no time decay of the production rate (Fig. 7d). To further improve practical applicability, we employ a simultaneous flow and evaporation strategy during long-term operation, instead of the conventional batch reaction. The evaporation device (a heater) is used to concentrate the produced H_2O_2 and is placed beneath the H_2O_2 accumulation tank. The H_2O_2 solution is continuously pumped out of the reactor at a rate of 0.2 mL min^{-1} and directly transferred to a Petri dish (diameter: 15 cm) maintained at 40 °C for concentration. After 50 h of continuous reaction, the accumulated volume of the concentrated H_2O_2 solution is approximately 25 mL, with a final H_2O_2 concentration of 100 mM (*ca.*

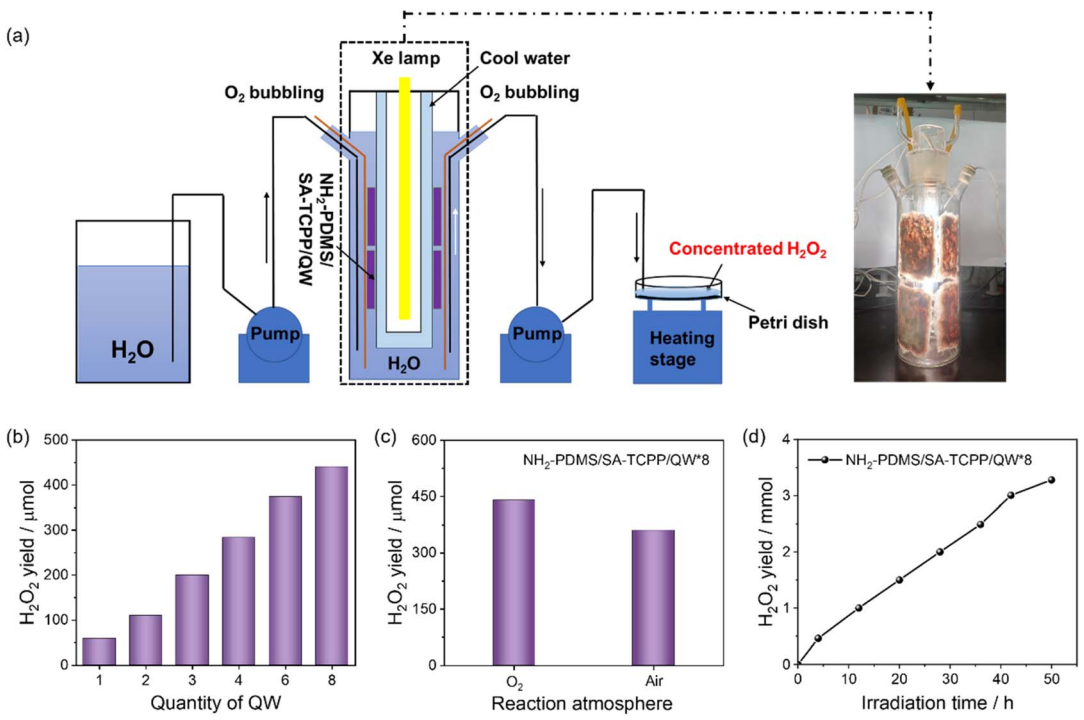

Fig. 7 (a) Schematic illustration of the continuous flow system for scale up H_2O_2 production using multiple QW modules and structural illustration of an internal-illumination reactor equipped with a centrally positioned Xe lamp and packed with NH_2-PDMS/SA-TCPP/QW composite (left). (b) Photocatalytic H_2O_2 production using different amount of QW modules. (c) Comparison of H_2O_2 production under pure O_2 and ambient air conditions using eight NH_2-PDMS/SA-TCPP/QW composite. (d) Time-dependent H_2O_2 production over 50 h of continuous operation. Solution: 350 mL H_2O, pH = 7, temperature: 40 °C, O_2 bubbling, reaction time: 4 h, light source: a 300 W long-arc Xe lamp with 400 nm.

0.3%). This value approaches the lower threshold of commercial concentrations (1–3%).

These findings demonstrate that the NH_2-PDMS/SA-TCPP/QW module maintains stable and efficient H_2O_2 production during scale-up experiments. The successful proof-of-concept validation of modular scale-up confirms the viability of a scalable and practical production strategy for H_2O_2. Additionally, we evaluate the economic feasibility of the H_2O_2 production on NH_2-PDMS/SA-TCPP/QW module. A detailed cost assessment is conducted based on an eight-module QW-supported laboratory system operating for 50 h (SI Note S5, Fig. S19a and Table S4). The total cost including the device, the materials, running and labor costs is approximately \$102.33 for the first 50 h run (0.12 g H_2O_2 production). The cost per gram of H_2O_2 is initially high (\$852.75 g^{-1}) at the lab scale, the device accounts for the vast majority of the total cost (92.2%). Due to the reusability of the device and the materials, 200 h long-time further reduces the cost to \$26.56 g^{-1} by considering only operational expenses with the device cost excluded. Compared with commercial-grade H_2O_2 (\$0.2–7.0 g^{-1} depending on the grade),[46] the current lab-scale cost of H_2O_2 production using the NH_2-PDMS/SA-TCPP/QW system remains relatively high, in the early stage, electricity, CH_2Cl_2, and SA-TCPP represent the major contributions (Fig. S19b), yet it holds substantial potential for cost reduction. For instance, substituting the Xe lamp with natural sunlight can eliminate electricity consumption, the major contributor to the operating, thereby reducing the estimated cost to approximately \$17.78 g^{-1} over 200 h. Scale-up operation can further reduce the cost of raw materials (*i.e.*, TCPP, QW, NH_2-PDMS, and CH_2Cl_2) and thus decreases the cost of H_2O_2 production from \$17.78 g^{-1} to \$8.37 g^{-1}. Moreover, if the photocatalytic activity is enhanced by an order of magnitude, the cost would decrease proportionally to one-tenth of the current level, approaching parity with the market price of commercial H_2O_2. Additional cost reductions are anticipated with further scale-up (Fig. S19c), which could bring the production price closer to that of high-value commercial products.

3. Conclusions

In summary, this study realizes the effective immobilization of self-assembled porphyrin nanosheets (SA-TCPP) on quartz wool (QW) *via* semi-solid PDMS interfacial engineering. The resulting PDMS/SA-TCPP/QW composite generates 95 μmol H_2O_2 in 4 h and exhibits stable photocatalytic performance for 10 reuse cycles. Its photocatalytic performance (7.4 mM) is comparable to that of the SA-TCPP powder (6.4 mM), with an internal quantum efficiency (IQE) as high as 15.84% at 420 nm. In a modular flow reactor, it generates 3.5 mmol H_2O_2 over 50 h and is concentrated to 100 mM by flow evaporation, which validates its potential for commercial-scale production. For PDMS/SA-TCPP/QW composite, the improved performance stems from synergistic physical encapsulation by high-viscosity PDMS and chemical fixation *via* amide bonding (–CONH–). This work provides an effective solution for the practical application of organic photocatalysts. These findings underscore the promising scalability and economic viability of this photocatalytic system for sustainable H_2O_2 production.

4. Experimental section

4.1. Materials

All chemicals and reagents are purchased of analytical grade and are used without further purification. Tetrakis(4-carboxyphenyl) porphyrin (TCPP, 97%) is purchased from Beijing InnoChem Technology Co., Ltd, China. Shanghai Mirel Chemical Technology Co., Ltd, China provides 1–3 μm high-purity quartz wool (QW) and polydimethylsiloxane (PDMS). Amino-modified and hydroxyl-modified polydimethylsiloxane (NH_2-PDMS/HO-PDMS) are provided by Dow Corning Co., Ltd, dichloromethane (CH_2Cl_2) and hydrochloric acid (HCl, 37 wt%) are purchased from Shanghai McLean Biochemical Technology Co., Ltd, China. Potassium hydroxide (KOH) is sourced from Sinopharm Chemical Reagent Co., Ltd, China.

4.2. Preparation of SA-TCPP

150 mg of TCPP is dissolved in 5 mL of 0.5 M KOH solution. The solution is stirred at room temperature for 0.5 h. Then, the alkaline TCPP solution is titrated with 0.1 M HCl using a constant-pressure separatory funnel until the pH reaches approximately 4.0. The resulting sample is centrifuged and washed three times with deionized water until the pH of the supernatant becomes neutral. The self-assembled TCPP powder (SA-TCPP) is collected and dried for 12 h at 60 °C.

4.3. Preparation of QW-loaded SA-TCPP catalyst

4.3.1. Pre-treatment of QW. The purchased QW is first immersed in 0.5 M NaOH solution for 0.5 h, and then heated at 80 °C for 1 h in a water bath. The pre-treated QW is washed with deionized water until the pH reaches 7.0, and then dried at 60 °C to remove impurities.

4.3.2. Loading of SA-TCPP onto QW. The prepared SA-TCPP is dispersed in 20 mL of dichloromethane and sonicated for 0.5 h. Then, 0.4 g of the pre-treated QW is added to the solution. The solution is evaporated at 60 °C to obtain the dried SA-TCPP/QW composite.

4.3.3. Preparation of the PDMS modified SA-TCPP/QW composite (PDMS/SA-TCPP/QW). To further improve the stability of the loading, a certain amount of PDMS is dissolved in 20 mL of dichloromethane, and then the prepared SA-TCPP is added. The mass ratio of SA-TCPP to PDMS ranges from 1 : 4 to 1 : 7. The suspension is sonicated for 0.5 h. Subsequently, the pre-treated QW is added to the well-dispersed suspension and the mixture is sonicated for an additional 0.5 h. The PDMS-containing suspension is evaporated at 60 °C to obtain the PDMS-modified SA-TCPP/QW composite, the composite contains SA-TCPP with a loading of approximately 45 wt% (SI Note S6, Fig. S20 and Table S5). NH_2-PDMS and HO-PDMS are prepared using the same method as pristine PDMS. They are named NH_2-PDMS/SA-TCPP/QW and HO-PDMS/SA-TCPP/QW composite, respectively. The amino groups in NH_2-PDMS are

identified by a colorimetric reaction with ninhydrin in ethanol to be 3.94 wt% (SI Note S7 and Fig. S21).

4.4. Characterizations

The SEM images are obtained using an S-4800 field emission scanning electron microscope (Hitachi, Japan). All FT-IR spectra are measured using a Nicolet 6700 Fourier-transform infrared spectrometer (Thermo Fisher Scientific, USA) within the range of 500–4000 cm^{-1}. TG and DTA data are collected on a TGA/DSC1/1100SF Thermal Analyzer (Mettler Toledo, Switzerland). The UV-Vis DRS absorption spectra are recorded by ultraviolet-visible (UV-Vis) spectroscopy using a UV-3600 plus ultraviolet-visible spectrophotometer (Shimadzu, Japan). The PDMS viscosity data are collected on an MCR302 Rotational Rheometer (Anton Paar GmbH). The contact angles of droplets of PDMS and H_2O on the PDMS/SA-TCPP/QW are measured using an OCA15EC contact angle meter (Dataphysics Instruments GmbH, Germany) at room temperature.

4.5. Photocatalytic production of H_2O_2

In the photocatalytic production of H_2O_2, 45 mg of SA-TCPP loaded onto QW modified with PDMS is placed in 30 mL of water in a quartz glass reactor, where O_2 is aerated for 20 minutes in the dark. The reactor is then placed in a temperature-controlled oil bath maintained at 40 °C. A Xe lamp (90 mW cm^{-2}, $\lambda \geq 420$ nm) is used as the light source.

The produced H_2O_2 concentration is determined by a potassium titanium oxalate method. At designated reaction intervals, 1 mL of the reaction solution is collected using a syringe topped with a 0.45 μm filter and mixed with 1 mL of prepared potassium titanium oxalate solution (0.02 M). The solution is observed to change from transparent to yellow due to the formation of a complex between potassium titanium oxalate and H_2O_2. The absorbance at 400 nm is used to determine the concentration of H_2O_2 and is monitored by a UV-Vis's spectrometer (UV-9010, Pushi, China).

Author contributions

J. L. carried out the investigation and visualization, and drafted the original manuscript. W. Q. contributed to validation and investigation. S. D. performed the IQE analysis. H. S. and Y. N. Z. conducted the SEM and FTIR measurements. J. X., J. Z., Y. Z., and Y. L. participated in data analysis and manuscript discussions. Y. Z. contributed to manuscript review and supervision. C. P. conceived the research idea, contributed to the conceptualization and methodology, oversaw writing—review and editing, provided resources, and supervised the project. All authors discussed the results, revised the manuscript, and approved the final version.

Conflicts of interest

The authors declare no competing interests.

Data availability

The data supporting this article have been included as part of the supplementary information (SI). Supplementary information: the SI includes additional material characterization data, activity results and experimental details. See DOI: **https://doi.org/10.1039/d5el00147a**.

Acknowledgements

This research is supported by the National Natural Science Foundation of China (22172065 and 22476071), Natural Science Foundation of Hebei Province (E2024210028). The authors also thank the Central Laboratory, School of Chemical and Material Engineering, Jiangnan University.

Notes and references

1 Y. Zhao, Y. Kondo, Y. Kuwahara, K. Mori and H. Yamashita, *Appl. Catal., B*, 2024, **351**, 123945.
2 H. Hou, X. Zeng and X. Zhang, *Angew. Chem., Int. Ed.*, 2020, **59**, 17356–17376.
3 M. Gu, D. Y. Lee, J. Mun, D. Kim, H. Cho, B. Kim, W. Kim, G. Lee, B. S. Kim and H. Kim, *Appl. Catal., B*, 2022, **312**, 121379.
4 Z. Yu, S. Li, Y. Wu, C. Ma, J. Li, L. Duan, Z. Liu, H. Sun, G. Zhao, Y. Lu, Q. Liu, Q. Meng and J. Zhao, *Green Chem.*, 2024, **26**, 9310–9319.
5 W. Yu, C. Hu, L. Bai, N. Tian, Y. Zhang and H. Huang, *Nano Energy*, 2022, **104**, 107906.
6 Y. Ding, S. Maitra, S. Halder, C. Wang, R. Zheng, T. Barakat, S. Roy, L. H. Chen and B. L. Su, *Matter*, 2022, **5**, 2119–2167.
7 L. Ding, Z. Pan and Q. Wang, *Chin. Chem. Lett.*, 2024, **35**, 110125.
8 X. Wang, Y. Shao, J. Pan, D. Jiang, Y. Cong and S. W. Lv, *Chem. Eng. J.*, 2024, **490**, 151923.
9 Y. He, Y. Wang, J. Qian, K. Xu, B. Lu, S. Tang, Y. Liu and J. Shen, *Appl. Catal., B*, 2025, **361**, 124565.
10 B. Lin, G. Yang, B. Yang and Y. Zhao, *Appl. Catal., B*, 2016, **198**, 276–285.
11 J. Jiang, Y. Liang, H. Wang, J. Zhao, J. Hu and M. Wang, *Fibers Polym.*, 2023, **24**, 1641–1648.
12 W. Li, F. Zhao, B. Zhu, X. Kong, X. Zhu and Q. Liu, *Adv. Compos. Hybrid Mater.*, 2020, **3**, 541–545.
13 Q. Liu, H. Zhou, J. Zhu, Y. Yang, X. Liu, D. Wang, X. Zhang and L. Zhuo, *Mater. Sci. Eng., C*, 2013, **33**, 4944–4951.
14 J. Zhang, Y. Du, L. Zhang, X. Zheng, Y. Ma, S. Dong and D. Zhou, *Mol. Catal.*, 2017, **432**, 1–7.
15 C. J. Chang, J. K. Chen, K. S. Lin, Y. H. Wei, P. Y. Chao and C. Y. Huang, *J. Alloys Compd.*, 2020, **813**, 152186.
16 X. Li, G. Zhang, N. Li, Q. Xu, H. Li, J. Lu and D. Chen, *Adv. Funct. Mater.*, 2024, **34**, 2316773.
17 S. Wang, Z. Xie, D. Zhu, S. Fu, Y. Wu, H. Yu, C. Lu, P. Zhou, M. Bonn, H. I. Wang, Q. Liao, H. Xu, X. Chen and C. Gu, *Nat. Commun.*, 2023, **14**, 6891.
18 Y. Kondo, Y. Kuwahara, K. Mori and H. Yamashita, *Chem*, 2022, **8**, 2924–2938.

19 T. Guo, H. Mashhadimoslem, L. Choopani, M. M. Salehi, A. Maleki, A. Elkamel, A. Yu, Q. Zhang, J. Song, Y. Jin and O. J. Rojas, *Small*, 2024, **20**, 2402942.
20 Y. Liu, L. Li, H. Tan, N. Ye, Y. Gu, S. Zhao, S. Zhang, M. Luo and S. Guo, *J. Am. Chem. Soc.*, 2023, **145**, 19877–19884.
21 J. Feng, Y. Wei, X. Li, Q. Wang, B. Wang, Y. Guo, B. Feng, E. Jin and J. Yu, *Angew. Chem., Int. Ed.*, 2025, e202508226.
22 C. Shen, Y. J. Wang, J. H. Xu and G. S. Luo, *Chem. Eng. J.*, 2012, **209**, 478–485.
23 X. Q. Gao, W. D. Lu, S. Z. Hu, W. C. Li and A. H. Lu, *Chin. J. Catal.*, 2019, **40**, 184–191.
24 L. Xiao, Y. Huang, Y. Luo, B. Yang, Y. Liu, X. Zhou and J. Zhang, *ACS Sustainable Chem. Eng.*, 2018, **6**, 14759–14766.
25 Z. Du, S. Zhang, C. Zhou, M. Liu and G. Li, *Talanta*, 2012, **94**, 104–110.
26 M. Saracino, L. Pretali, M. L. Capobianco, S. S. Emmi, M. L. Navacchia, F. Bezzi, C. Mingazzini, E. Burresi and A. Zanelli, *Water Sci. Technol.*, 2018, **77**, 409–416.
27 M. Grześkowiak, R. J. Wróbel, D. Moszyński, S. Mozia, J. Grzechulska Damszel, A. W. Morawski and J. Przepiórski, *Adsorpt. Sci. Technol.*, 2014, **32**, 765–773.
28 M. Na and N. L. Zhou, *Carbohydr. Polym.*, 2014, **105**, 70–74.
29 Y. He, N. Cheshomi and S. M. Lawson, *Chem. Eng. J.*, 2021, **410**, 128326.
30 S. Lteif, N. A. Nosratabad, S. Wang, Y. Xin, S. J. Weigand, H. Mattoussi and J. B. Schlenoff, *Langmuir*, 2023, **39**, 15748–15755.
31 S. A. Sonawane, K. B. Kulkarni, M. L. Bari, U. D. Patil, J. S. Narkhede and T. D. Deshpande, *Silicon*, 2024, **16**, 5097–5108.
32 R. S. Calolsa, T. P. Sumangala, S. K. Kalpathy, T. Thomas, M. U. Kahaly and A. Rahaman, *J. Appl. Polym. Sci.*, 2025, **142**, e57014.
33 Y. Shao, Y. Zhang, C. Chen, S. Dou, Y. Lou, Y. Dong, Y. Zhu and C. Pan, *Chin. J. Catal.*, 2024, **61**, 205–214.
34 Y. Zhang, C. Pan, G. Bian, J. Xu, Y. Dong, Y. Zhang, Y. Lou, W. Liu and Y. Zhu, *Nat. Energy*, 2023, **8**, 361–371.
35 W. Chen, Z. Luo, H. Chen, H. Kuang and D. Liu, *J. Chem. Res.*, 2012, **36**, 72–74.
36 T. Poursaberi, M. Hassanisadi, K. Torkestani and M. Zare, *Chem. Eng. J.*, 2012, **189–190**, 117–125.
37 L. Palacios-Pineda, I. Perales-Martinez, L. Lozano-Sanchez, O. Martínez-Romero, J. Puente-Córdova, E. Segura-Cárdenas and A. Elías-Zúñiga, *Polymers*, 2017, **9**, 696.
38 A. Yazdan, J. Wang, C. W. Nan and L. Li, *J. Electron. Mater.*, 2020, **49**, 2100–2109.
39 Y. Li, J. Cheng, P. Lu, W. Guo, Q. Wang and C. He, *Food Anal. Methods*, 2017, **10**, 1922–1930.
40 M. A. Ahmed, B. M. Felisilda, A. Wuethrich and J. P. Quirino, *J. Chromatogr., A*, 2021, **1657**, 462553.
41 L. Brown, M. J. Earle, M. A. Gîlea, N. V. Plechkova and K. R. Seddon, *Top. Curr. Chem.*, 2017, **375**, 74.
42 K. Hayashi, M. Nakamura, H. Miki, S. Ozaki, M. Abe, T. Matsumoto, T. Kori and K. Ishimura, *Adv. Funct. Mater.*, 2014, **24**, 503–513.
43 B. Cao, Y. Liu, Y. Zhao, J. Qu, Q. Zhou, F. Xiao, C. Li, L. Wang and R. Li, *Angew. Chem., Int. Ed.*, 2025, **64**, e202422495.
44 C. Zhang, M. Cao, S. Jiang, X. Huang, K. Yan and K. Mai, *Int. J. Polym. Anal. Charact.*, 2019, **24**, 40–53.
45 J. Yue, H. Yang, C. Liu, S. Wang and X. Kang, *Chem. Eng. J.*, 2024, **497**, 154683.
46 H_2O_2, price, Sigma-Aldrich, **https://www.sigmaaldrich.com/US/en/search/H2O2**, accessed Sep 09, 2025.